Article

Oxide Additive-Free α- → β-Si_3N_4 Phase Transformation at 1900 °C

Hisayuki Imamura , Kazuhiro Kura , Tsunehiro Kawata , Sawao Honda , Toru Asaka , Yuji Iwamoto *

Posted Date: 12 October 2023

doi: 10.20944/preprints202310.0817.v1

Keywords: Silicon nitride; Phase transformation; Oxygen impurity; Metastable solid solution; Grain boundary

Article

Oxide Additive-Free α- → β-Si_3N_4 Phase Transformation at 1900 °C

Hisayuki Imamura [1,2], Kazuhiro Kura [2], Tsuneniro Kawata [2], Sawao Honda [1], Toru Asaka [1] and Yuji Iwamoto [1,*]

[1] Department of Life Science and Applied Chemistry, Graduate School of Engineering, Nagoya Institute of Technology, Gokiso-cho, Showa-ku, Nagoya 466-8555, Japan; h.imamura.927@stn.nitech.ac.jp (H.I.); honda@nitech.ac.jp (S.H.); toru.asaka@nitech.ac.jp (T.A.); iwamoto.yuji@nitech.ac.jp (Y.I.)

[2] Global Research and Innovative Technology Center, Proterial Ltd., 5200, Mikajiri, Kumgaya, Saitama 360-8577, Japan; kazuhiro.kura.bd@proterial.com (K.K.) ; tsunehiro.kawata.nr@proterial.com.

* Correspondence: iwamoto.yuji@nitech.ac.jp; Tel.: +81-52-735-5276

Abstract: Oxide additive-free α- → β-Si_3N_4 phase transformation of a high-purity commercial α-Si_3N_4 powder was investigated at 1600 to 1900 °C under nitrogen pressure of 980 kPa. The XRD analysis revealed that the α- → β-Si_3N_4 phase transformation proceeded mainly at 1900 °C, and was completed by the extensive 1900 °C-heat treatment for 20 h. This phase transformation temperature was 33 °C lower than the theoretical α-Si_3N_4 dissociation temperature and confirmed as completely different from that often discussed for the liquid phase sintering of α-Si_3N_4 powder by direct comparison with the phase transformation behavior of a reference powder, α-Si_3N_4 powder doped with 1 mol% Y_2O_3. The unique α- → β-Si_3N_4 phase transformation was further studied by a set of characterization techniques including elemental analysis, HAADF-STEM and STEM-EDS analyses. The results strongly suggested that the oxide additive-free α- → β-Si_3N_4 phase transformation was governed by the formation of metastable solid solution between α-Si_3N_4 and impurity oxygen of approximately 0.6 wt%, which promoted the dissociation below the theoretical α-Si_3N_4 dissociation temperature to afford thermodynamically favorable β-Si_3N_4. Along with the β-Si_3N_4 formation, the impurity oxygen was concentrated at the Si_3N_4 crystal grain boundaries and subsequently released from the sample via the grain boundary diffusion.

Keywords: silicon nitride; phase transformation; oxygen impurity; metastable solid solution; grain boundary

1. Introduction

Because of their high thermal conductivity and excellent mechanical properties, silicon nitride (Si_3N_4) ceramics have been successfully applied as insulated substrates in the semiconductor power modules mounted on inverters assembled in Electric Vehicle (EV) and Hybrid Electric Vehicle (HEV) [1,2]. The material properties of Si_3N_4 ceramics are closely related to their microstructures, and a bi-modal structure composed of fine matrix Si_3N_4 grains and elongated large grains is ideal for harmonizing high fracture strength and toughness as well as high thermal conductivity [3–5]. For fabricating such high-performance β-Si_3N_4 ceramics, the rod-like β-Si_3N_4 seeding to starting α-Si_3N_4 powders is a practical way to construct the bi-modal structure composed of fine matrix grains and selectively grown elongated grains originating from the seed crystallites through the liquid phase sintering [6–8]. Regarding the method for preparing rod-like β-Si_3N_4 seed crystallites, Hirao et al. [9] reported the procedure with several steps as follows: (i) heat treatment of α-Si_3N_4, yttria (Y_2O_3) and silica (SiO_2) mixed powders at 1850 °C under N_2 gas pressure of 0.5 MPa to afford rod-like β-Si_3N_4 polycrystallites with Si-Y-O-N glassy phase, (ii) pulverizing the aggregates using a mortar and pestle, (iii) glass phase dissolution by acid treatment followed by neutralization treatment and cleaning, (iv) classifying the resulting isolated seed crystallites and (v) drying. On the other hand, recently, we proposed a facile method to produce rod-like β-Si_3N_4 seed crystallites by the oxide additive-free

 doi:10.20944/preprints202310.0817.v1

single-step heat treatment at 1900 °C of commercial α-Si_3N_4 powder [10–12]. Subsequently, the bi-modal structure controlling was successfully achieved for the liquid phase-sintered β-Si_3N_4-MgO (1 wt%)-Re_2O_3 (3 wt%) (R = Gd, Yb, Y, La) ceramics by the addition of 10 vol% rod-like β-Si_3N_4 seeds produced at our laboratory, and the resulting ceramics sintered at 1900 °C for 40 h exhibited improved thermal conductivity of higher than 110 $Wm^{-1}K^{-1}$ [13].

Generally, it is accepted that the α- → β-Si_3N_4 phase transformation proceeds through the dissolution-precipitation process in the oxynitride liquid phase formed *in-situ* at the heat treatment temperature [14,15] and besides the oxide additives [16–18], the initial contents of free silicon [19] and β-Si_3N_4 phase in the starting α-Si_3N_4 powder [20] have been reported as additional factors to accelerate the formation of β-Si_3N_4. On the other hand, the oxide additive-free α- → β-Si_3N_4 phase transformation has been reported for fully densified Si_3N_4 ceramics fabricated by high-pressure sintering of α-Si_3N_4 powder using techniques such as hot isostatic pressing (HIP) [21–24] and high-pressure and high-temperature (HPHT) sintering [25]. Hou et al. [25] reported that micron-size α-Si_3N_4 was transformed into submicron-sized polycrystallites β-Si_3N_4 under the HPHT condition at 5.5 GPa and temperatures ranging from 1600 to 1900 °C, and the α- → β-Si_3N_4 phase transformation was found to complete at 1900 °C for 3 min. As a possible mechanism for the observed phase transformation, the nucleation-growth mechanism of liquid-solid phase transformation was suggested since the observed α- → β-Si_3N_4 phase transformation proceeded at around the melting point of Si_3N_4 under high pressure [25,26]. The high-resolution TEM observation of the sample fabricated by the HPHT sintering revealed full-phase transformation from α- to β-Si_3N_4, while the β-Si_3N_4 crystal grain boundaries were free from secondary crystalline or glassy phase, *i.e.*, there was no evidence for the eutectic liquid-phase formation during the HPHT sintering [25,26].

In our previous study [12], the correlation between the α- → β-Si_3N_4 phase transformation behavior and the changes in the amount of oxygen and carbon impurities, and the α- → β-Si_3N_4 phase transformation kinetics at 1900 °C were investigated under nitrogen pressure of 980 kPa. Our analytical results revealed that the experimentally observed α- → β-Si_3N_4 phase transformation was suggested to be promoted by the formation of metastable solid solution between the impurity oxygen and α-Si_3N_4 followed by decomposition and release of oxygen-containing volatile species to afford β-Si_3N_4 [12].

In the present study, to investigate the unique phase transformation in more detail, the oxide additive-free α- → β-Si_3N_4 phase transformation at 1600 to 1900 °C is directly compared with the reference powder sample of α-Si_3N_4 doped with 1 mol% yttrium oxide (Y_2O_3) in which the α- → β-Si_3N_4 phase transformation can be promoted via the liquid phase [27]. Subsequently, the oxide additive-free Si_3N_4 powder samples with various β-phase content are prepared by varying the heat treatment duration time at 1900 °C. The correlation between the α- → β-Si_3N_4 phase transformation behavior and changes in the oxygen-impurity content of the selected Si_3N_4 crystal grains of both α- and β-phase and those of their two-grain boundaries is investigated and discussed based on the results obtained by a set of characterization techniques including elemental analysis, X-ray diffraction (XRD), transmission electron microscopy (TEM), high-angle annular dark-field scanning TEM (HAADF-STEM), STEM-energy dispersive X-ray spectroscopy (EDS) and **electron backscatter diffraction** (EBSD) analyses.

2. Experimental procedures

2.1. Starting powders and heat treatment condition

Commercially available α-Si_3N_4 powder (grade SN-E10, Ube Industries, Ltd., Tokyo, Japan) was used as-received. The specific surface area (SSA), mean particle size (d_{50}) and β-phase content are 11.0 m^2g^{-1}, 0.9 μm and 3.73 %, respectively. The total metal impurity, oxygen and carbon impurity contents are less than 50 ppm, 1.23 and 0.11 wt%, respectively. As a comparison study, to observe the α- → β-Si_3N_4 transformation through the liquid phase, Y_2O_3 powder (grade UU-type, purity, 99.9 %, SSA: 15.9 m^2g^{-1}, d_{50}: 0.5 μm, Shin-Etsu Chemical, Co. Ltd., Fukui, Japan) [28] as used as an oxide additive: As-received α-Si_3N_4 powder (labeled as **E10**) was mixed with 1 mol% Y_2O_3 powder and ball milled in

Preprints (www.preprints.org) | NOT PEER-REVIEWED | Posted: 12 October 2023 doi:10.20944/preprints202310.0817.v1

ethanol for 2 h and dried at 80 °C for 5 h under a flowing nitrogen (N_2). The resulting mixed powder was labeled as **E10 +1 mol% Y_2O_3**.

A prescribed amount of the **E10** and **E10+1 mol% Y_2O_3** sample powders were placed in a boron nitride (BN) crucible and heat-treated in a graphite resistance-heated furnace (Model High Multi 5000, Fuji Dempa Kogyo, Co., Ltd., Osaka, Japan) at selected temperatures from 1600 to 1900 °C for 5 h under N_2 gas pressure of 980 kPa. In addition, the effect of the 1900 °C heat-treatment duration time on the morphology and α- → β-Si_3N_4 phase transformation was studied for up to 20 h.

2.2. Characterizations

The evaluation of oxygen and carbon impurities and the β-phase content of the powder samples was conducted in the same manner as described in our previous report [12].

Morphologies of the powder samples were observed by using a scanning electron microscope (SEM, Model JSM-7900F, JEOL Ltd., Tokyo, Japan.

In this study, TEM/HAADF-STEM, STEM-EDS and EBSD analyses were intensively performed on the powder samples to investigate the α- → β-Si_3N_4 transformation behavior associated with the changes in the oxygen impurity contents within the Si_3N_4 crystal grains and those at their grain boundaries. TEM specimens were prepared by focused ion beam (FIB) techniques (Model FB-2100, JEOL Ltd., Tokyo, Japan): The powder sample was embedded within epoxy resin and maintained under vacuum for 5 min by using a rotary pomp. Then, the pressure was returned to atmospheric pressure and the mixed compound was cured at room temperature for 12 h. The cured compound composed of the powder sample and resin was mechanically pre-polished. The pre-polished surface of the cured compound was covered with tungsten (W) protective thin film, then the resulting compound was transferred to the FIB equipment for final thinning.

The TEM and HAADF-STEM observations were carried out by using an atomic resolution analytical electron microscope with a STEM Cs corrector incorporated as standard (Model JEM-ARM200F, JEOL Ltd., Tokyo, Japan) operating at an acceleration voltage of 200 kV, which allows to perform the HAADF-STEM observation at a high resolution of 78 pm.

EDS analysis was conducted in the STEM mode with a spectrometer (Model JED-2300T, JEOL Ltd., Tokyo, Japan) mounted on the atomic resolution analytical electron microscope. Selected area electron diffraction (SAED) analysis was performed to identify the unit cell structure whether α-Si_3N_4 or β-Si_3N_4 phase and the symmetries (crystal axis and face orientation) of the Si_3N_4 phase.

In this study, HAADF-STEM analysis for determining the atomic configuration in the vicinity of the Si_3N_4 grain boundary was performed under the operation conditions as previously discussed by Clarke and Thomas [29] and conducted by Kleebe et al. [30,31] and Kim et al. [32]: The crystal grain boundary has to be tilted in an edge-on position to the incident beam. Furthermore, the crystal grain boundary should be flat with a low density of interfacial steps, and the crystal grains on either side of the grain boundary should be aligned in an orientation suitable for structure imaging or at least for forming one set of lattice fringes.

In this study, the α-Si_3N_4 crystal grains in the heat-treated powder sample with an especially high β-phase content of 96.5 % were identified by the EBSD analysis (Model Aztec HKL Advanced Symmetry, Oxford Instruments Holdings 2013 Inc., Tokyo, Japan with application equipment: Model Map Sweeper, Oxford Instruments Holdings 2013 Inc., Tokyo, Japan). The EBSD measurements were carried out in low vacuum operating mode which eliminated the coverage of the surface since the gas ionized by the electrons was capable of neutralizing the surface charges. A High-resolution EBSD image on an approximately 6 × 4 μm² area of the sample TEM specimen was obtained under the operation condition with a step size of 20 nm and an acceleration voltage of 20 kV.

3. Results and discussion

3.1.α-→β-. Si_3N_4 phase transformation behaviors

3.1.1. Morphological changes and β-phase content

Preprints (www.preprints.org) | NOT PEER-REVIEWED | Posted: 12 October 2023 doi:10.20944/preprints202310.0817.v1

As a reference, the morphologies of the starting α-Si_3N_4 and Y_2O_3 powders used in this study are shown in Figure 1.

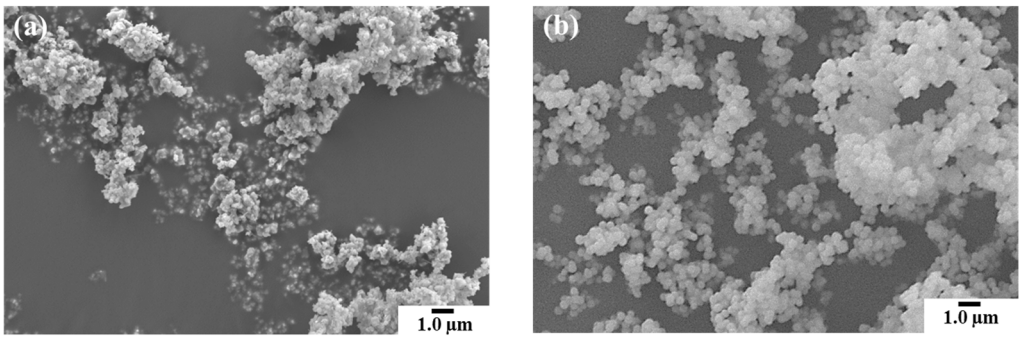

Figure 1. SEM images showing the morphology of as-received starting powders of (a) Si_3N_4 and (b) Y_2O_3.

The morphology changes and the α- → β-Si_3N_4 phase transformation behaviors during the heat treatment up to 1900 ℃ of the **E10** and **E10+1 mol% Y_2O_3** powder samples are summarized and shown in Figure 2 and Figure 3(a), respectively. The addition of 1 mol%-Y_2O_3 promoted Si_3N_4 elongated grain growth at 1700 to 1800 ℃ (Figs. 2(b) and 2(c)) associated with the completion of α- → β-Si_3N_4 phase transformation at 1800 ℃ (Figure 3(a)), which are consistent with those previously observed during the liquid-phase sintering of Si_3N_4-Y_2O_3-SiO_2 system [33]. On the other hand, even after the 1900 ℃ -heat treatment for 5 h, the **E10** sample kept the equiaxed morphology (Figure 2(f)), and the β-Si_3N_4 phase content remained below 25 % (Figure 3(a)). As we reported previously [12], continuous grain growth proceeded during the extended 1900 °C-heat treatment for up to 20 h to afford hexagonal rod-like grains (Figs. 2(g) to 2(i)). Moreover, β-Si_3N_4 phase content increased consistently with the 1900 °C-heat treatment time to reach 100 % at 20 h (Figure 3(b)).

Preprints (www.preprints.org) | NOT PEER-REVIEWED | Posted: 12 October 2023 doi:10.20944/preprints202310.0817.v1

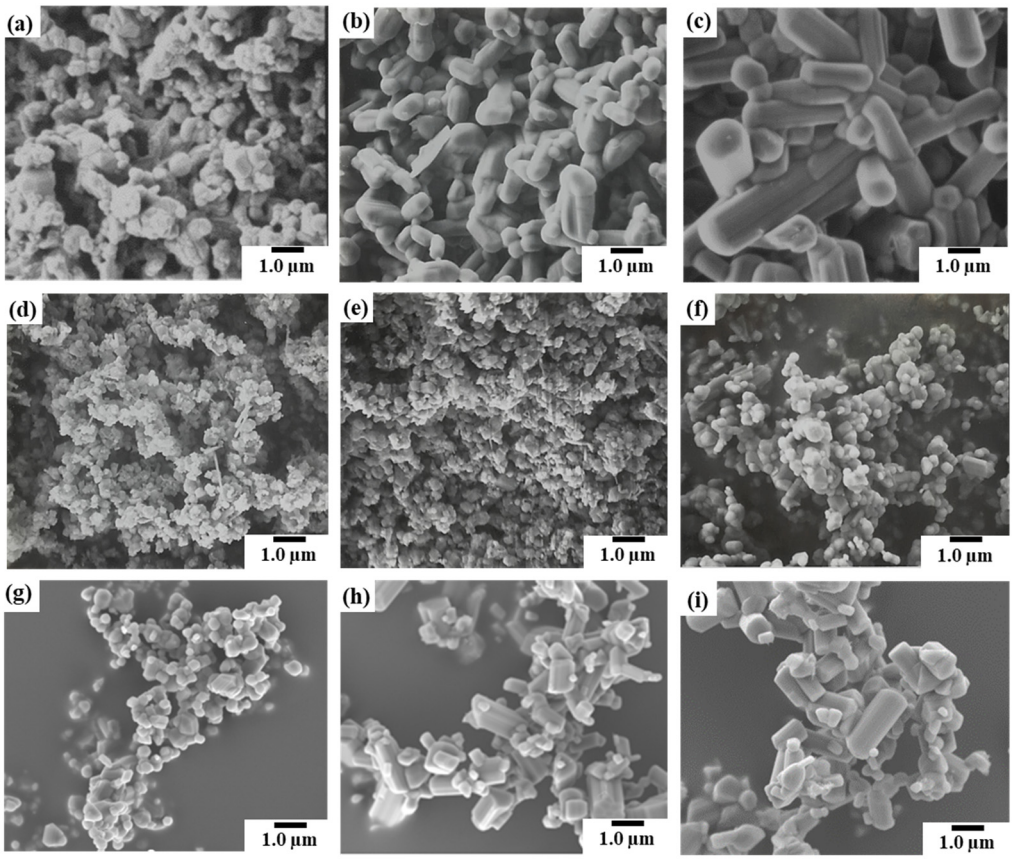

Figure 2. Morphologies of sample powders: (a-c) **E10+1 mol% Y_2O_3** and (d-i) **E10**. Heat treatment condition: (a), (d) 1600 °C for 5 h, (b), (e) 1800 °C for 5 h, (c), (f) 1900 °C for 5 h, and 1900 °C for (g) 12 h, (h) 18 h and (i) 20 h.

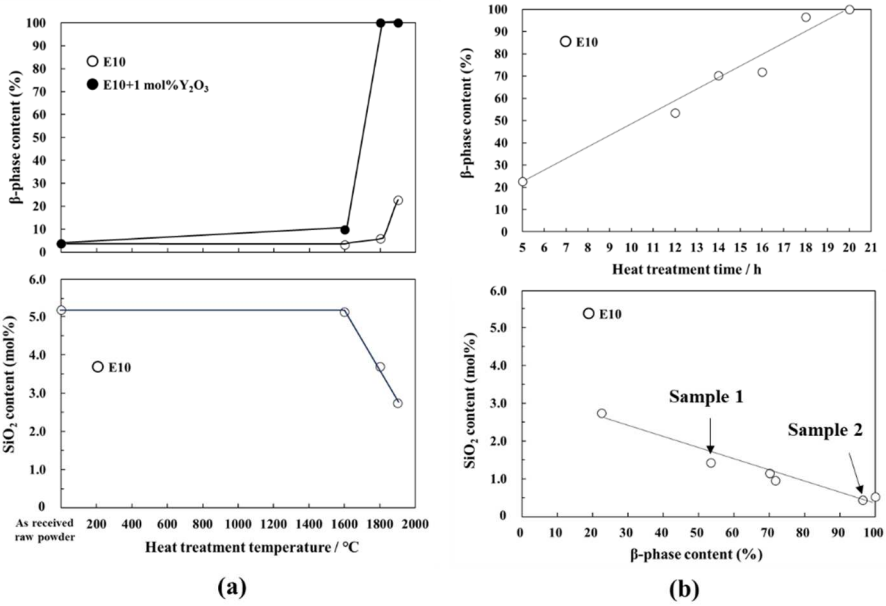

Figure 3. (a) Correlation between the heat treatment temperature for 5 h and β-phase content and SiO_2 impurity content of **E10** and **E10+1 mol% Y_2O_3** power samples. (b) Correlation between the heat treatment time at 1900 °C and β-phase content and the relation between β-phase content and SiO_2 impurity content of the **E10** powder sample.

3.1.2. Relation between chemical composition and β-phase content

 doi:10.20944/preprints202310.0817.v1

The oxygen (O) and carbon (C) impurity contents of as-received and heat-treated α-Si_3N_4 powder samples are listed in Table S1. The contents of O impurity calculated as SiO_2 (mol %) [12] are plotted as a function of heat treatment temperature and 1900 °C-heat treatment time in Figs. 3(a) and 3(b), respectively.

After the 5 h-heat treatment up to 1900 °C, the SiO_2 and C contents decreased from 5.17 to 2.74 mol% and 1.23 to 0.8 mol%, respectively (Figure 3(a) and Table S1). Accordingly, the observed increase in the β-Si_3N_4 phase content at 1600 to 1900 °C was suggested by the β-Si_3N_4 formation via carbothermal nitridation reaction between the impurity C and SiO_2 generally recognized as a surface oxide layer formed by the impurity oxygen (Eq. (1)) [34]. As another possible route for the β-Si_3N_4 formation, silicon oxynitride (Si_2N_2O) formation and decomposition (Eq. (2) [35]) could be considered since Si_2N_2O was suggested as another possible phase at 1600 to 1800 °C according to the phase diagrams of the binary SiO_2-Si_3N_4 system [36,37].

$$3SiO_2\,(s) + 6C\,(s) + 2N_2\,(g) \rightarrow \beta\text{-}Si_3N_4\,(s) + 6CO\,(g) \qquad (1)$$

$$3Si_2N_2O\,(s) \rightarrow \beta\text{-}Si_3N_4\,(s) + N_2\,(g) + 3SiO\,(g)\ (T > 1750\ °C) \qquad (2)$$

During the extended 1900 °C-heat treatment for up to 20 h, both the SiO_2 and C contents decreased consistently with the heating time (Table S1), which revealed that the carbothermal nitridation (Eq. (1)) continuously proceeded, however, this contribution to the increase in the β-Si_3N_4 phase content was essentially small since the amounts of the SiO_2 and C after the 1900 °C-heat treatment for 5 h were as low as 0.64 wt% (2.74 mol% as SiO_2) and 0.07 % (0.8 mol%), respectively (Table S1). It should also be noted that the silicon oxynitride liquid phase formation was excluded at such low SiO_2 contents [36,37].

The experimental results obtained in the present study clearly revealed that the dominant mechanism for the α- → β-Si_3N_4 phase transformation of the E10 sample at 1900 °C was intrinsically different from that generally discussed for the liquid phase sintering of Si_3N_4 ceramics [38]. In this study, we focused on the role of impurity oxygen in the α- → β-Si_3N_4 phase transformation, and the relation between the α- → β-Si_3N_4 transformation behavior and the change in the oxygen impurity content shown in Figure 3(b) was further studied.

3.2. Nanostructure characterization by HAADF-STEM and STEM-EDS analyses

3.2.1. Phase identification

The changes in the oxygen impurity contents within the Si_3N_4 crystal grains and their two-grain boundaries were intensively studied by the HAADF-STEM observation combined with STEM-EDS analysis. In this study, two powder samples with apparently different β-Si_3N_4 phase content of 53.5 and 96.5 % were selected and labeled as Sample 1 and Sample 2, respectively, as shown in Figure 3(b).

First, HAADF-STEM analysis was performed on the selected Si_3N_4 crystal grains for the assignment of α- and β-phase and the identification of the three different kinds of two-grain boundaries, α/α-phase, α/β-phase and β/β-phase.

(a) Sample 1 with β-phase content of 53.5 %

A typical TEM image of the Sample 1 is shown in Figure 4(a). Within this image, two grains labeled **G1** and **G2** were selected.

The HAADF-STEM image of the **G1** and the SAED pattern shown in Figure 4(b) corresponded to the plane orientation adjusted to the [0001] zone axis of α-Si_3N_4. Analogously, that of the **G2** shown in Figure 4(c) corresponded to the plane orientation adjusted to the $[01\bar{1}1]$ zone axis of α-Si_3N_4. Accordingly, the two-grain boundary between the **G1** and **G2** (**GB1/2**) was assigned as α/α-phase.

Preprints (www.preprints.org) | NOT PEER-REVIEWED | Posted: 12 October 2023 doi:10.20944/preprints202310.0817.v1

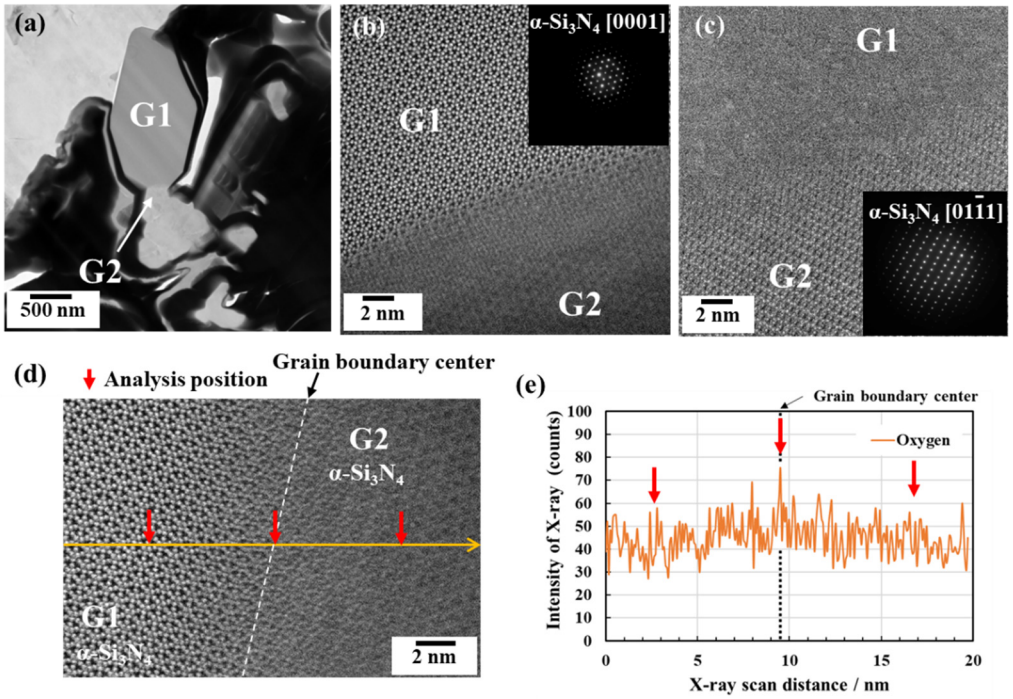

Figure 4. Results of nanostructure characterization for Sample 1 with β-phase content of 53.5 %. (a) Low magnification TEM image (The dark contrast surrounding the Si_3N_4 grains corresponds to the protective compound (see experimental section, 2.2. Characterizations)) and HAADF-STEM image and SAED pattern of the Si_3N_4 crystal grain labeled **G1** (b) and **G2** (c) shown in (a). (d) HAADF-STEM image showing near the two-grain boundary of the **G1** and **G2**, and (e) STEM-EDS line analysis for oxygen element performed on the orange line shown in (d).

Further nanostructure characterization was performed on Sample 1 and the results are summarized and shown in Figure 5. Three grains labeled **G3**, **G4** and **G5** in the BF-STEM image shown in Figure 5(a) were selected. The HAADF-STEM image and the SAED pattern analyses resulted in assigning the **G3** as α-Si_3N_4 (Figs. 5(b)) and the **G4** as β-Si_3N_4 (Figs. 5(c)), while the **G5** (Figure 5(d)) exhibited a typical HAADF-STEM image of the basal plane observed from the [0001] direction of β-Si_3N_4 [39], indicating the **GB3/4** and **GB3/5** as α/β-phase.

On the other hand, the selected grain labeled **G6** in the BF-STEM image in Figure 5(e) exhibited a typical HAADF-STEM image of the prismatic plane observed from the [10$\bar{1}$0] direction of β-Si_3N_4 [40] (Figure 5(f)), and those labeled **G7** and **G8** in Figure 5(e) were also assigned as β-Si_3N_4 (Figs. 5(g) and (h)), thus it was identified that both the **GB6/7** and **GB6/8** as β/β-phase.

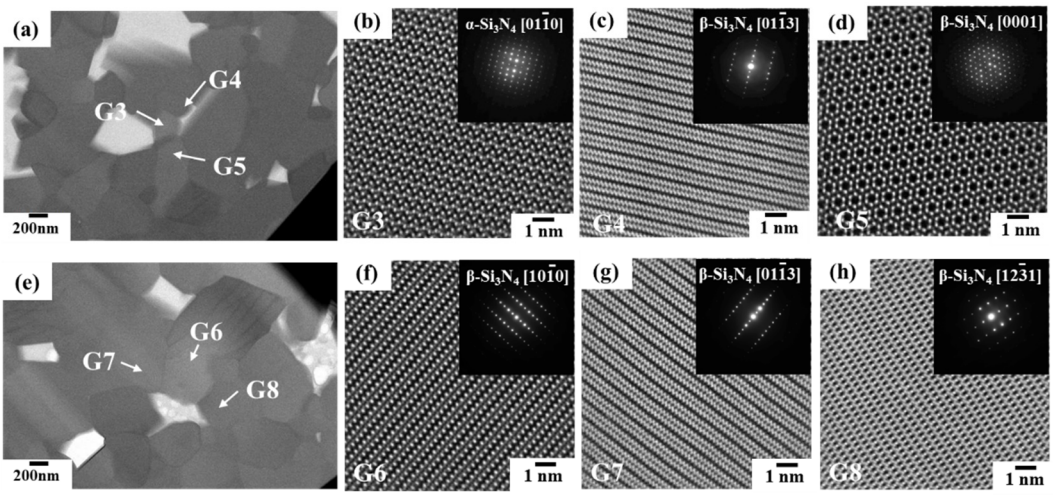

Preprints (www.preprints.org) | NOT PEER-REVIEWED | Posted: 12 October 2023 doi:10.20944/preprints202310.0817.v1

Figure 5. Results of phase identifications for the crystal grains in Sample 1 with β-phase content of 53.5 %. (a) and (e) Typical BF-STEM images showing Si_3N_4 polycrystallites. HAADF-STEM image and SAED pattern of the Si_3N_4 crystal grain labeled **G3** (b), **G4** (c) and **G5** (d) shown in (a), and those of grain labeled **G6** (f), **G7** (g) and **G8** (h) shown in (e).

(b) Sample 2 with β-phase content of 96.5 %

To find out α-Si_3N_4 crystal grains and the two-grain boundary of α/β-phase in Sample 2 with a high β-phase content of 96.5 %, the TEM-EBSD analysis was performed as shown in Figure 6(a) in which the yellow colored and blue colored grains were β-Si_3N_4 and α-Si_3N_4, respectively. Within the matrix composed of β-Si_3N_4 grains, the α-Si_3N_4 grains were located randomly, and their grain sizes were in the range of about 0.2 to 0.8 μm, while those of β-Si_3N_4 grains were approximately 0.15 to 1.00 μm.

Based on the results obtained by the EBSD combined with BF-STEM analyses (Figs. 6(a) and (b)), three grains labeled **G9**, **G10** and **G11** were selected and confirmed as α-Si_3N_4, β-Si_3N_4 and β-Si_3N_4, respectively (Figs. 6(c) to 6(e)). As a result, both the **GB9/10** and **GB9/11** were assigned as α/β-phase. Further analysis was performed for several two-grain boundaries in Sample 2, and as a typical result, the BF-STEM image, HAADF-STEM image, and SAED pattern of the selected grains labeled **G12** and **G13** were shown in Figure 7.

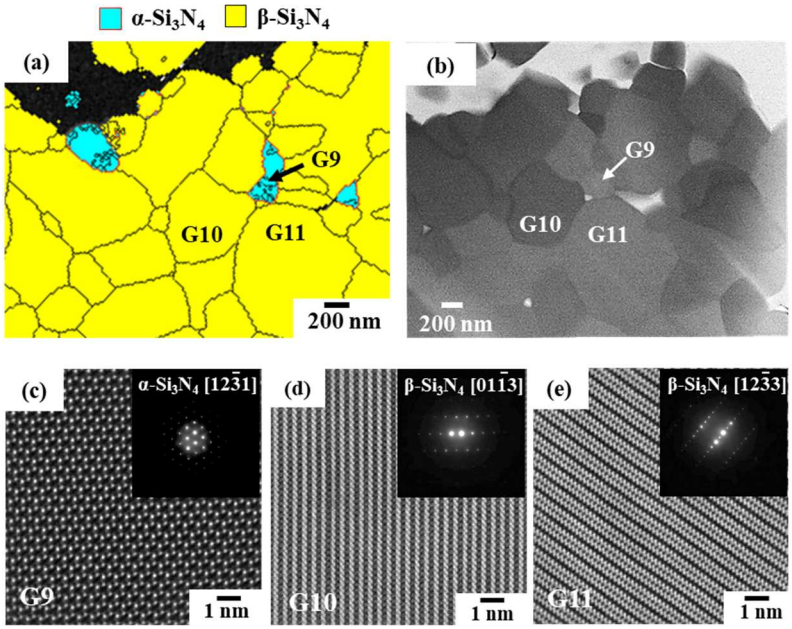

Figure 6. (a) TEM-EBSD analysis performed on Sample 2 with β-phase content of 96.5 %. Yellow- and blue-colored grains indicate β-Si_3N_4 and α-Si_3N_4, respectively. (b) BF-STEM observation for the area analyzed by the TEM-EBSD analysis. HAADF-STEM image and SAED pattern of the Si_3N_4 crystal grain labeled **G9** (c), **G10** (d) and **G11** (e) shown in (b).

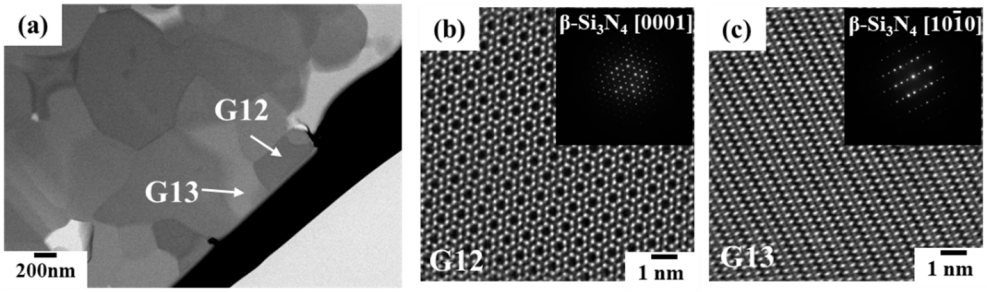

Figure 7. Results of phase identifications for the crystal grains in Sample 2 with β-phase content of 96.5 %. (a) Typical BF-STEM images showing Si_3N_4 polycrystallites. HAADF-STEM image and SAED pattern of the Si_3N_4 crystal grain labeled **G12** (b) and **G13** (c).

Preprints (www.preprints.org) | NOT PEER-REVIEWED | Posted: 12 October 2023 doi:10.20944/preprints202310.0817.v1

3.2.2. Oxygen impurity contents within Si_3N_4 crystal grains and at two-grain boundaries

Figures 4(d) and (e) show a HAADF-STEM image near the α/α-phase grain boundary between the **G1** and **G2** (**GB1/2**), and the result of STEM-EDS line scanning analysis to detect the changes in the O element near the grain boundary of the two grains, respectively. The HAADF-STEM image showed no obvious existence of glassy phases at the two-grain boundary, however, the detective count for O element was highest at the X-ray scan distance of 9.5 nm. Then, this position was fixed as the center of the two-grain boundary, and for measuring the oxygen impurity content, the STEM-EDS analysis was performed for the square area with 4.0 nm width and 8.0 nm length in each Si_3N_4 crystal grain, **G1** and **G2** as well as for the square area with 0.3 nm width and 2.0 nm length in the two-grain boundary, **GB1/2** (Figure S1(a)). The center position of the former square sites was set at 7 nm from the center of the two-grain boundary as indicated by the red arrows in Figs. 4(d) and (e).

The spectra obtained by the STEM-EDS area analysis for the **G1**, **G2** and **GB1/2** are shown in Figure S2. The O element was detected as a minor peak in each spectrum, and the impurity O contents of the **G1**, **G2** and **GB1/2** were evaluated as 1.2, 1.0 and 1.0 wt%, respectively (Table S2).

A set of the HAADF-STEM observation near the two-grain boundary accompanied by the STEM-EDS line scanning and area analysis for O element was performed on all the labeled grains **G3** to **G13** and their two-grain boundaries (Figures 8, 9 and S1).

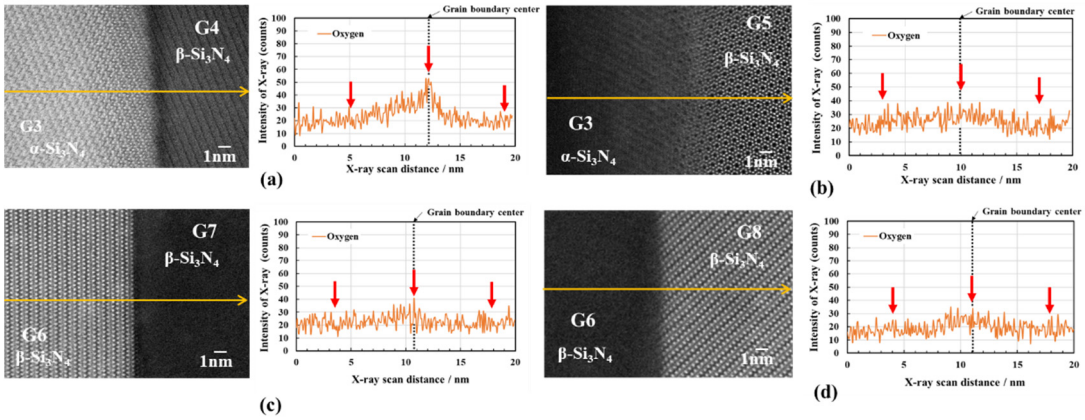

Figure 8. Results of HAADF-STEM image and STEM-EDS line analyses for oxygen element performed on the area near the two-grain boundary of the labeled grains of (a) **G3** and **G4**, (b) **G3** and **G5**, (c) **G6** and **G7** and (d) **G6** and **G8** in Sample 1. Red arrows indicate the center position of the area analyzed by the STEM-EDS analysis for measuring oxygen content shown in Figure S2.

The HAADF-STEM image near the two-grain boundary **GB3/4** shown in Figure 8(a) revealed the **G3** and **G4** grains in the edge-on condition. Here, when the grain boundary was under edge-on conditions, the incident direction of the electron beam was under off-Bragg conditions for each grain. On the other hand, it was difficult to obtain an edge-on condition for the grain boundary **GB3/5**, therefore, the observation was conducted by adjusting to the orientation of the **G5** grain from the [0001] direction of β-Si_3N_4 crystal to obtain the clear image as shown in Figure 5(d).

Analogously, the HAADF-STEM image analyses for the area nearby the **GB6/7** (Figure 8(c)) and **GB6/8** (Figure 8(d)) were conducted by adjusting to the orientation of the **G6** grain [$10\bar{1}0$] direction of β-Si_3N_4 crystal to obtain clear images as shown in Figure 5(f), and those for the area nearby the **GB9/10** (Figure 9(a)) and **GB9/11** (Figure 9(b)) were conducted by adjusting to the orientation of the grain **G9** [$12\bar{3}1$] direction of β-Si_3N_4 crystal to obtain clear image as shown in Figure 6(c). On the other hand, the HAADF-STEM image analysis for the area near the **GB12/13** were conducted by adjusting to the orientation of the grain **G13** [$10\bar{1}0$] direction of β-Si_3N_4 crystal to obtain a clear image as shown in Figure 9(c).

Preprints (www.preprints.org) | NOT PEER-REVIEWED | Posted: 12 October 2023 doi:10.20944/preprints202310.0817.v1

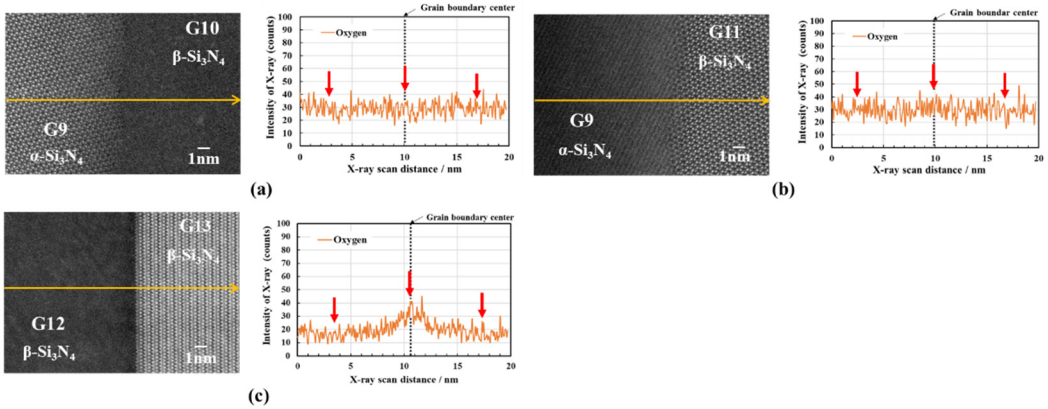

Figure 9. Results of HAADF-STEM image and STEM-EDS line analyses for oxygen element performed on the area near the two-grain boundary of the labeled grains of (a) **G9** and **G10**, (b) **G9** and **G11** and (c) **G12** and **G13** in Sample 2. Red arrows indicate the center position of the area analyzed by the STEM-EDS analysis for measuring oxygen content shown in Figure S2.

All the HAADF-STEM images showed no obvious existence of glassy phases at the two-grain boundary. Then, the impurity O contents were evaluated in the same manner as shown in Figure S1. The impurity O contents are listed in Table S2 and compared with those for the **G1**, **G2**, and **GB1/2** in Figure 10.

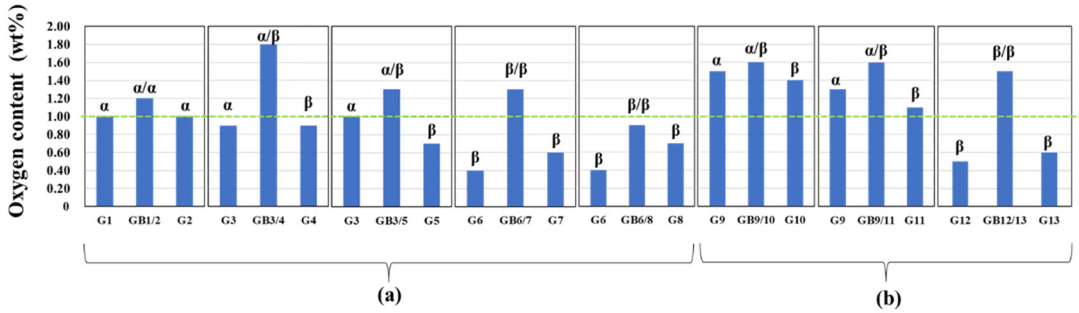

Figure 10. Oxygen contents in Si_3N_4 crystal grains and their two-grain boundaries evaluated for (a) Sample 1 with a β-phase content of 53.5 % and (b) Sample 2 with a β-phase content of 96.5 % by STEM-EDS analysis.

Due to the low impurity O contents (Table S1), It was indeed difficult to precisely evaluate the amount of impurity O by the present STEM-EDS area analysis. In this study, the relative difference in the amount of the impurity O was discussed for the samples. The results obtained for Sample 1 suggest that, regardless of the phase combination, impurity O content at the two-grain boundary is higher than those within the two Si_3N_4 crystal grains (Figure 10(a)). Sample 2 in which the β-phase content reaches 96.5% (Figure 10(b)) also shows a similar tendency, however, the impurity O contents measured for the Si_3N_4 crystal grains are varied: In Sample 1, the impurity O contents in the β-Si_3N_4 crystal grains are 0.4 to 0.9 wt% and found to be lower than those measured for the α-Si_3N_4 crystal grains (approximately 1.0 wt%). On the other hand, in Sample 2, in addition to the α-Si_3N_4 crystal grain **G9** (1.5 wt%), particular β-Si_3N_4 crystal grains such as the **G10** and **G11** which form two-grain boundary with the α-Si_3N_4 crystal grain **G9** exhibit relatively high impurity O content above 1.0 wt%, while other β-Si_3N_4 crystal grains such as **G12** and **G13** show much lower impurity O contents of 0.5 and 0.6 wt %, respectively.

The experimental results obtained in the present study suggest that the impurity oxygen was initially distributed uniformly both in the α-Si_3N_4 crystal grains and at the grain boundaries. Then, the 1900 °C -heat treatment promoted oxygen diffusion from Si_3N_4 crystal grains to their grain boundaries associated with the α- → β-phase transformation of the α-Si_3N_4 crystal grains.

 doi:10.20944/preprints202310.0817.v1

Around the final stage of the α- → β-phase transformation reaching 96.5 % β-phase (Figure 10(b)), the impurity O seemed to be concentrated within the local area composed of α-Si_3N_4 crystal grain remained, the β-Si_3N_4 crystal grains surrounding the α-Si_3N_4 crystal grain and their two-grain boundaries. The α-Si_3N_4 crystal grain might act as an oxygen scavenger to increase the impurity O content within the local area since α-Si_3N_4 has been reported as an oxygen-stabilized phase in an approximate formula of $Si_{11.5}N_{15}O_{0.5}$ [41,42]. However, the subsequent oxygen diffusion from the β-Si_3N_4 crystal grains to their grain boundaries proceeded, which reduced the resulting impurity O content in the β-Si_3N_4 crystal grains as low as 0.5 to 0.6 wt%. The impurity O concentrated at the grain boundaries was thought to be released from the sample via the grain boundary diffusion, and the resulting total impurity O content of the powder sample measured by the inert gas fusion method [12] was reduced to 0.12 wt% (Table S1).

3.3. *Role of impurity oxygen in α- → β-Si_3N_4 phase transformation*

It has been suggested that the formation of α-Si_3N_4 is attributed to kinetic reasons and metastable compared to β-Si_3N_4 [43,44]. As one possible pathway for the α- → β-Si_3N_4 phase transformation, Zakorzhevskii suggested that, at low impurity O content (0.5 to 0.7 wt%), the impurity O dissolves into the crystal lattice of α-Si_3N_4 to afford a metastable solid solution [45] which is the driving force of α- → β-Si_3N_4 phase transformation below the theoretical α-Si_3N_4 dissociation temperature [36]:

$$\alpha\text{-}Si_3N_4\ \text{crystal} \rightarrow 3Si + 2N_2\ (\text{dissociation}) \rightarrow \beta\text{-}Si_3N_4\ \text{crystallization} \quad (3)$$

The impurity O content of the **E10** sample powder after the 1900 °C -heat treatment for 5 h was as low as 0.64 wt% (2.74 mol% as SiO_2), and thus silicon oxynitride liquid phase formation was excluded at such low SiO_2 content [37,38], indeed the 1900 °C -heat treated powder samples exhibited clear Si_3N_4 crystal grain boundaries without secondary glassy phases (Figs. 4, 8 and 9), and the final impurity O content after the 1900 °C-heat treatment for 20 h reduced to be 0.12 % (Table S1). Moreover, the α- → β-Si_3N_4 phase transformation experimentally observed in the present study proceeded mainly at 1900 °C under N_2 pressure of 980 kPa, which was 33 °C lower than the theoretical α-Si_3N_4 dissociation temperature (1933 °C [46]). These results strongly suggest that the oxide additive-free α- → β-Si_3N_4 phase transformation observed in our present study is dominantly governed by the reaction Eq. (4) promoted by the metastable solid solution formation between the oxygen impurity (SiO_2) and α-Si_3N_4 followed by dissociation to afford thermodynamically favorable β-Si_3N_4 accompanied by the release of oxygen.

$$\alpha\text{-}Si_3N_4\ \text{crystal} + xSiO_2 \rightarrow \text{metastable solid solution} \rightarrow [3Si + 2N_2 + 1/2xO_2] \rightarrow \beta\text{-}Si_3N_4\ \text{crystal} + 1/2xO_2\uparrow \quad (4)$$

4. Conclusions

In this study, high-purity commercial α-Si_3N_4 powder with an initial β-phase content of 3.7 %, total metal impurities below 50 ppm, and oxygen and carbon impurity contents of 1.23 and 0.11 wt%, respectively was used to investigate the oxide additive-free α- → β-Si_3N_4 phase transformation at 1600 to 1900 °C under nitrogen pressure of 980 kPa. The results can be summarized as follows:

(1) The α- → β-Si_3N_4 phase transformation was found to proceed mainly at 1900 °C, and the extensive heat treatment for up to 20 h achieved full transformation to afford rod-like β-Si_3N_4 polycrystallites. This transformation temperature was found to be 33 °C lower than the theoretical α-Si_3N_4 dissociation temperature.

(2) The impurity O contents of the powder samples after the 1900 °C -heat treatment for 5 h and 20 h were measured to be 0.64 and 0.12 wt %, respectively. At such lower oxygen contents, the silicon oxynitride liquid phase formation at 1900 °C was excluded according to the phase diagram reported for the binary Si_3N_4-SiO_2 system.

(3) The HAADF-STEM, as well as the STEM-EDS analyses performed on the 1900 °C heat-treated powder samples, also revealed no evidence for the formation of the secondary crystalline or glassy phases at the Si_3N_4 two-grain boundaries.

(4) The HAADF-STEM/STEM-EDS analyses performed on the area near the two-grain boundary

clarified that, at the β-phase content of 53. 5 %, regardless of the phase combination, the impurity oxygen content at the two-grain boundary was higher than those within the two Si_3N_4 crystal grains.

(5) As a possible dominant mechanism, the oxide additive-free α-→β-Si_3N_4 phase transformation at 1900 °C was suggested to be governed by the formation of metastable solid solution between the α-Si_3N_4 and the impurity oxygen remained at approximately 0.6 wt%, which promoted the dissociation below the theoretical α-Si_3N_4 dissociation temperature to afford thermodynamically favorable β-Si_3N_4. Along with the β-Si_3N_4 formation, the impurity oxygen was concentrated at the Si_3N_4 crystal grain boundaries and subsequently released from the sample via the grain boundary diffusion.

Supplementary Materials: The following supporting information can be downloaded at the website of this paper posted on Preprints.org. **Figure S1**: Position of areas within the Si_3N_4 crystal grains and at the two-grain boundary selected for measuring the oxygen content by TEM-EDS analysis. (a) **G1** and **G2**, (b) **G3** and **G4**, (c) **G3** and **G5**, (d) **G6** and **G7**, (e) **G6** and **G8**, (f) **G9** and **G10**, (g) **G9** and **G11**, and (d) **G12** and **G13**.; **Figure S2:** The spectra obtained by the STEM-EDS area analysis for (a) grain **G1**, (b) grain **G2**, and (c) the two-grain boundary between **G1** and **G2** (**GB1/2**).; **Table S1**: Impurity oxygen and carbon contents and β-phase content evaluated for Si_3N_4 powder samples.; **Table S2**: Silicon, nitrogen and oxygen contents in Si_3N_4 crystal grains and their two-grain boundaries evaluated by STEM-EDS analysis.

Author Contributions: Conceptualization, H.I.; methodology, H.I. K.K. and T.K.; investigation, H.I. K.K. and T.K.; Formal analysis, S.H. and T.A.; writing—original draft preparation, H.I.; writing—review and editing, Y.I.; supervision, Y.I. All authors have read and agreed to the published version of the manuscript.

Funding: The authors did not receive support from any organization for this work.

Conflicts of Interest: The authors declare no conflict of interest.

References

1. Yang, Y.; Gomba, L. D.; Rodriguez, R.; Mak, C.; Emadi, A. Automotive Power Module packing: Current Status and Future Trends. IEEE Access. **2020**, 8, 160126-160144, **doi.** 10.1109/ACCESS.2020.3019775
2. Mustain, H. Si_3N_4 SUBSTRATE FOR HYBRID / ELECTRIC VEHICLE DRIVE TRAIN INVERTER POWER MODULE Design-to-cost Si_3N_4 Ag-free AMB Metal Ceramic Substrate. Heraeus Electronics – Battery Show North America. September **2022**, PowerPoint Presentation (thebatteryshow.com)https://www.thebatteryshow.com/content/dam/Informa/amg/novi/2022/docs/14_45%20-%20Mustain.pdf
3. Hirao, K.; Nagaoka, T.; Brito, M. E.; Kanzaki, S. Microstructure Control of Silicon Nitride by Seeding with Rodlike β-Silicon Nitride Particles. J. Am. Ceram. Soc.**1994**, 77, 1857-1862, doi. org/10.1111/j.1151-2916.1994.tb07062.x
4. Imamura, H.; Hirao, K.; Brito, M. E.; Toriyama, M.; Kanzaki, S. Further Improvement in Mechanical Properties of Highly Anisotropic Silicon Nitride Ceramics. J. Am. Ceram. Soc. **2000**, 83, 495-500, doi .org/10.1111/j.1151-2916.2000.tb01223.x
5. Yokota, H.; Ibukiyama, M. Effect of the addition of β-Si_3N_4 nuclei on the thermal conductivity of β-Si_3N_4 ceramics. J. Eur. Ceram. Soc. **2003**, 23, (8), 1183-1191**,** doi.org/10.1016/S0955-2219(02)00292-3
6. Liang, Z. H.; Zhang, H.; Gui, L.; Li, J.; Peng, G.; Jiang, G. Effects of whisker-like β-Si_3N_4 seeds on phase transformation and mechanical properties of α to β-Si_3N_4 composites using $MgSiN_2$ as additives. Ceram Int. 2013, 39, 2743-2751, doi.org/10.1016/j.ceramint.2012.09.041
7. Dai, J.; Li, J.; Chen, Y.; Yang, L.; Sun, G. Preparation of the rod-like β-Si_3N_4 particles favoring the self-reinforcing Si_3N_4 ceramics. Mater. Res. Bull. **2003**, 38, 609-615, doi.org/10.1016/S0025-5408(03)00023-0
8. Vućković, A.; Bošković, S.; Matović, B.; Vlajić, M.; Krstic, V. Effect of β- Si_3N_4 seeds on densification and fracture toughness of silicon nitride. Ceram. Int. **2006**, 32, 303-307, doi.org/10.1016/j.ceramint.2005.02.015
9. Hirao, K.; Tsuge, A.; Brito, M.E.; Toriyama, M.; Kanzaki, S. Preparation of Rod-like β-Si_3N_4 Single Crystal Particles. J. Ceram. Soc. Japan. **1993**, 101, 1078-1080, doi.org/10.2109/jcersj.101.1078

10. Imamura, H.; Kawata, T.; Sobue, M. Hitachi Metals Co. ltd., Methods for producing silicon nitride and silicon nitride sintered specimens and circuit boards using them. Japanese Patent 3775335. **2006**, March, 3.
11. Imamura, H.; Kawata, T.; Sobue, M. Hitachi Metals Co. ltd., Methods for producing silicon nitride and silicon nitride sintered specimens and circuit boards using them. Japanese Patent 4518020. **2010**, May, 28.
12. Imamura, H.; Kawata, T.; Honda, S.; Iwamoto, Y. A facile method to produce rodlike β-Si_3N_4 seed crystallites for bimodal structure controlling. J. Am. Ceram. Soc. **2023**, 106, (3), 1694-170.
13. Imamura, H.; Kawata, T.; Honda, S.; Iwamoto, Y. Thermal conductivity improvement in Si_3N_4 ceramics via grain purification. J. Am. Ceram. Soc. in press, doi.org/10.1111/jace.19478
14. Sarin, V. K. On the α-to-β Phase Transformation in Silicon Nitride. Mater. Sci. Eng. **1998**, A105, (106), 151-159, doi.org/10.1016/0025-5416(88)90491-0
15. Goto, Y.; Thomas, G. Phase Transformation and Microstructure Change of Si_3N_4 During Sintering. J. Mater. Sci. **1995**, 30, 2194-2200, doi.org/10.1007/BF01184561
16. Greskovich, C.; Prochazka, S. Observation on the $\alpha \rightarrow$ β-Si_3N_4 transformation. J. Am. Ceram. Soc. **1977**, 60, (9-19), 471-472, doi.org/10.1111/j.1151-2916.1977.tb15542.x
17. Bowen, L. J.; Weston, R. J.; Carruthers, T. G.; Brook, R. J. Hot-pressing and α-β phase transformation ins silicon nitride. J. Mater. Sci. **1978**, 13, 341-350, doi.org/10.1007/BF00647779
18. Kim, J. R.; Kim, C. H. Effects of ZrO_2 and Y_2O_3 dissolved zyttrite on the densification and the α/β phase transformation of Si_3N_4 in Si_3N_4-ZrO_2 composite. J. Mater. Sci. **1990**, 25, 493-498, doi.org/10.1007/BF00714062
19. Park, J. Y.; Kim, J. R.; Kim, C. H. Effects of free silicon on the α to β phase transformation in silicon nitride. J. Am. Ceram. Soc. **1987**, 70, (10), C240-C242, doi.org/10.1111/j.1151-2916.1987.tb04886.x
20. Messier, D. R.; Riley, F. L.; Brook, R. J. The α/β Silicon Nitride Phase Transformation. J. Mater. Sci. **1978**, 13, 1119-1205, doi.org/10.1007/BF00544725
21. Homma, K.; Okada, H.; Fujikawa, T.; Tatuno, T. HIP sintering of silicon nitride without additives. Yogyo-Kyokai-Shi. **1987**, 95, 299-234, doi.org/10.2109/jcersj1950.95.1098_229
22. Tanaka, I.; Pezzotti, G.; Miyamoto, Y.; Okamoto, T. Fracture toughness of Si_3N_4 and its Si_3N_4 whisker composite without sintering aids. J. Mater. Sci. **1993**, 28, 4217-4222, doi.org/10.1007/BF00576053
23. Tanaka, I.; Pezzotti, G.; Okamoto, T.; Miyamoto, Y.; Koizumi, M. Hot isostatics press sintering and properties of silicon nitride without additives. J. Am. Ceram. Soc. **1989**, 72, 1656-1660, doi.org/10.1111/j.1151-2916.1989.tb06298.x
24. Lu, P.; Danforth, S. C.; Symons, W. T. Microstructure and grain-boundary characterization of HIP'ed high-purity silicon nitride. J. Mater. Sci. **1993**, 28, 4217-4222, doi.org/10.1007/BF00351257
25. Hou, Z.; Wang, H.; Yang, Y.; Song, X.; Chen, S.; Wan, B. S.; Zhao, X.; Shang, M.; Chen, B. High-pressure synthesis of high-performance β-Si_3N_4 bulk without additives, Ceram. Int. **2020**, 46, 12449-12457, doi.org/10.1016/j.ceramint.2020.02.007
26. Bradley, R. S.; Murnro, D. C.; Whitfield, M. The reactively and polymorphism of selected nitrides at high temperatures and high pressures. J. Inorg. Nucl. Chem. **1966**, 1803-1812, doi.org/10.1016/0022-1902(66)80266-X
27. Pejryd, L. The Effect of Temperature and Yttria Content on the Properties of Hot Isostatically Pressed Si_3N_4. Mater. Sci. and Eng. 1988, A105/106, 169-174, doi.org/10.1016/0025-5416(88)90493-4
28. Shin-Etsu Chemical Co.,Ltd. [homepage on the internet]. Production Introduction of Rare-Earth Oxides. Available from https://www.rare-earth.jp/en/product.html
29. Clarke, D. R.; Thomas, G. Grain Boundary Phases in a Hot-Pressed MgO Fluxed Silicon Nitride. J. Am. Ceram. Soc. **1995**, 60, (11-12), 491-494, doi.org/10.1111/j.1151-2916.1977.tb14089.x
30. Kleebe, H. J.; Cinibulk, M. K.; Cannon, R. M.; Rühle, M. Statistical Analysis of the intergranular Film Thickness in Silicon Nitride Ceramics. J. Am. Ceram. Soc. **1993**, 76, (8), 1969-1977, doi.org/10.1111/j.1151-2916.1993.tb08319.x
31. Kleebe, H. J. Structure and Chemistry of interface in Si_3N_4 Ceramics Studied by TEM. J. Ceram. Soc. Japan. **1997**, 105, (6), 453-475, doi.org/10.2109/jcersj.105.453
32. Kim, S. K.; Zhang, Z.; Kasiser, U. Local symmetry braking of a thin crystal structure of β-Si_3N_4 as revealed by spherical aberration corrected high-resolution transmission electron microscopy images. J. Electron. Micro. **2012,** 61, (3), 145-157, doi.org/10.1093/jmicro/dfs038

33. Babini, G. N.; Bellosi, A.; Vincenzini, P. Densification and α-β Transformation Mechanisms During Hot Presing of Si_3N_4-Y_2O_3-SiO_2 Compositions. Mater. Chem. Phys. **1984**, 11, 365-400, doi.org/10.1016/0254-0584(84)90040-3
34. Yang, J.F.; Shan, S.Y.; Janssen, R.; Schneider, G.; Ohji, T.; Kanzaki, S. Synthesis of fibrous β-Si_3N_4 structured porous ceramics using carbothermal nitridation of silica. Acta. Mater. **2005**, 53, 2981-2990, doi.org/10.1016/j.actamat.2005.03.011
35. Zakorzhevskii, V. V. Effect of Oxygen Impurities and Synthesis Temperature on the Phase Composition of the Products of Self-Propagating High-Temperature Synthesis of Si_3N_4. Inorg. Mater. **2018**, 54, 349-353, doi.org/10.1134/S0020168518040143
36. Weiss, J.; Lukas, H. L; Lorenz, J.; Petzow, G.; Krieg, H. Calculation of heterogeneous phase equilibria in oxide-nitride systems:I.The quaternary system C-Si-N-O. Calphad: Comput Coupling Phase Digar Thermochem. **1981**, 5, (2), 125-140, doi.org/10.1016/0364-5916(81)90039-0
37. Hillert, M.; Jonsson, S.; Sundman, B. Thermodynamic Calculation of the Si-N-O system, Z. Metallkd. **1992**, 83, (9), 648-654, doi.org/10.1515/ijmr-1992-830902
38. Dai, J.; Li, J.; Chen, Y. The phase transformation behavior of Si_3N_4 with single Re_2O_3 (Re = Ce, Nd, Sm, Eu, Gd, Dy, Er, Yb) additive. Mater. Chem. Phys. **2003**, 80, 356-359, doi.org/10.1016/S0254-0584(02)00519-9
39. Hiraga, K.; Tsuno, K.; Shindo, D.; Hirabayashi, M.; Hayashi, S.; Hirai, T. Structure of α- and β-Si_3N_4 observed by 1MV electron microscopy. Philos. Mag. A. **1983**, 47, (4), 483-489, doi.org/10.1080/01418618308245241
40. Ziegler, A.; Kisielowski, C.; Hoffmann, M. J.; Ritchie, R. O. Atomic Resolution Transmission Electron Microscopy of the intergranular Structure of a Y_2O_3-containing Silicon Nitride Ceramic. J. Am. Ceram. Soc. **2003**, 86, (10), 1777-1785, doi.org/10.1111/j.1151-2916.2003.tb03554.x
41. Riley, F. L. Silicon nitride and related materials. J. Am. Ceram. Soc. **2000**, 83, 245-265, doi.org/10.1111/j.1151-2916.2000.tb01182.x
42. Priest, H. H.; Burns, F. C.; Priest, G. L.; Skaar E. C. The Oxygen Content of Alpha Silicon Nitride. J. Am. Ceram. Soc. **1973**, 56, (7), 395, doi.10.1111/j.1151-2196.1973.tb12700.x
43. Seiferit, H. J.; Peng, J. Q.; Lukas, H. L. Aldinger F. Phase equilibria and thermal analysis of Si-C-N ceramics, J. Alloy. Compd. **2001**, 320, 251-261, doi.org/10.1016/S0925-8388(00)01478-X
44. Xu, B.; Dong, J.; McMillan, P. F.; Shebanova, O.; Salamat, A. Equilibrium and metastable phase transitions in silicon nitride at high pressure: a first-principles and experimental study. Phys. Rev. B. **2011**, 84, 014113, doi.org/10.1103/PhysRevB.84.014113
45. Liang, J. J.; Topor, L.; Navrotsky, A.; Mitomo, M. Silicon Nitride: enthalpy of formation of α and β-polymorphs and the effect of C and O impurities. J. Mater. Res. **1999**, 14, 1959-1968, doi.org/10.1557/JMR.1999.0264
46. Iwamoto, Y. PhD thesis: Microstructure Control of Si-based Non-Oxide Ceramics through Precursor Design, p. 86, Graduate School of Frontier Sciences, Department of Advanced Materials Science: The University of Tokyo. **2004**, doi.org/10.15083/0002002800